

Optical Polarization Characteristics of Low-Earth-Orbit Space Targets

Zhenduo ZHANG*

*Navigation College, Dalian Maritime University, Dalian 116026, China and
Environmental Information Institute, Dalian Maritime University, Dalian 116026, China*

Yuanhao WU and Zhengwei LI

*Changchun Institute of Optics, Fine Mechanics and Physics,
Chinese Academy of Sciences, Changchun 130033, China*

(Received 6 September 2019; revised 24 October 2019; accepted 24 October 2019)

This study investigates the optical polarization characteristics of low-earth-orbit (LEO) space targets at different operating attitudes for different surface materials by analyzing these characteristics using a microfacet analysis model. Subsequently, the polarization image of a typical LEO space target was simulated, and several laboratory and outfield polarization detection experiments were conducted. Simulated and experimental results validate the effectiveness of polarization in analyzing and evaluating the operating attitudes of the LEO space targets and in identifying their material properties. Results show that the polarization images can effectively determine the constituent structure of the LEO space targets.

PACS numbers: 42.25.Ja, 42.30.-d, 42.68.Mj

Keywords: Polarization image, LEO space target, Optics, Modeling analysis

DOI: 10.3938/jkps.76.311

I. INTRODUCTION

The demand for ground-based detection and recognition of low-earth-orbit (LEO) space targets is increasing daily worldwide. Therefore, further improvements in the detection ability and the accurate acquisition of the important characteristic information about the LEO space targets, such as the target's task, structural composition, surface material, and operating attitudes, require new detection techniques and methods. Polarization is another inherent property of light and is an optical information dimension independent of the intensity, wavelength, and coherence; it reflects the optical characteristics of a target from a new perspective. When polarization is combined with other features of light, such as the light intensity, spectrum, and image, its attributes and behaviors can be more accurately understood because several dimensions of optical information together represent the same target [1–10].

Currently, the polarization characteristics of LEO space targets and their polarization imaging characteristics have not been investigated sufficiently. The polarization characteristics of LEO space targets can be accurately detected owing to the rapid development of high-precision polarizer technology [11,12], polarization-preserving optical element coating technology, and polar-

ization system design and calibration technology. The polarization image of LEO space targets can be accurately detected using a ground-based large-aperture telescope because of the development of large-aperture telescope manufacturing technology [13–18], adaptive optics technology [19–23], and atmospheric transmission impact analysis technology [24,25].

This study discusses, analyzes, and validates the effectiveness of the detection of LEO space target polarization. Section II presents the microfacet analysis model employed for analyzing the polarization characteristics of LEO space targets. These characteristics will be analyzed for different operating attitudes and surface materials in Sections III and IV, respectively. Section V provides the results of the polarization image simulation analyses of the targets whereas Section VI describes and discusses the laboratory and outfield polarization imaging experiments. Section VII generalizes the importance of polarization detection in LEO space target detection and recognition.

II. POLARIZATION CHARACTERISTIC ANALYSIS MODEL

The surface of a LEO space target can be considered as containing a cluster of small microfacets in different normal directions. The microfacet model described in a

*E-mail: zhenduo69@163.com

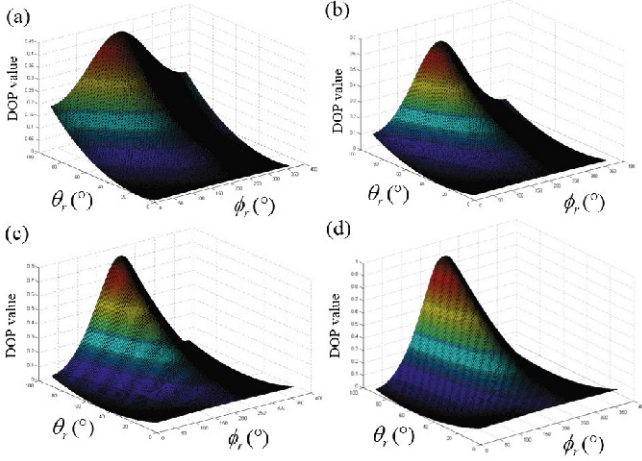


Fig. 2. (Color online) Solar panel polarization characteristics with sunlight incident at angles of (a) $(15^\circ, 0^\circ)$, (b) $(30^\circ, 0^\circ)$, (c) $(45^\circ, 0^\circ)$, and (d) $(60^\circ, 0^\circ)$.

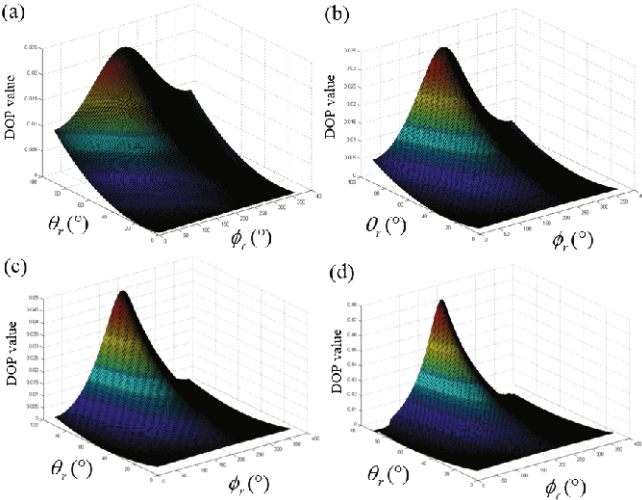


Fig. 3. (Color online) Main body polarization characteristics with sunlight incident at angles of (a) $(15^\circ, 0^\circ)$, (b) $(30^\circ, 0^\circ)$, (c) $(45^\circ, 0^\circ)$, and (d) $(60^\circ, 0^\circ)$.

III. POLARIZATION CHARACTERISTICS OF THE LEO SPACE TARGETS WITH DIFFERENT OPERATING ATTITUDES

Based on the polarization characteristic analysis model, we selected the incident sunlight angles (θ_i, ϕ_i) as $(15^\circ, 0^\circ)$, $(30^\circ, 0^\circ)$, $(45^\circ, 0^\circ)$, and $(60^\circ, 0^\circ)$ for the simulation and analysis of the polarization characteristics of the satellite solar panel and its main body. The results are presented in Figs. 2 and 3, in which we could clearly observe the following:

1. The DOP value is symmetrically distributed at $\phi_i = 0^\circ$ about $\phi_r = 180^\circ$ for both the satellite solar panel and the main body.

2. The DOP value varies with the receiving zenith and azimuth angles, *i.e.*, θ_r and ϕ_r , respectively, for both the

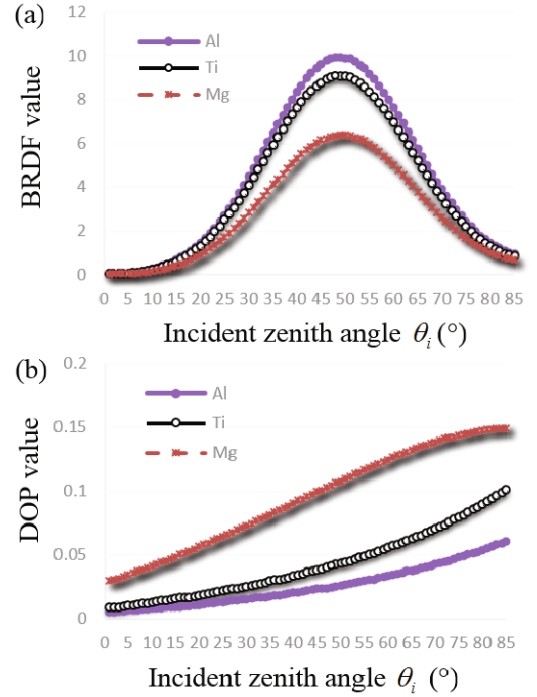


Fig. 4. (Color online) (a) BRDF and (b) DOP analyses results for different materials as functions of the incident zenith angle.

satellite solar panel and the main body.

3. An increase in the sunlight's incident zenith angle θ_i corresponds to an increase in the DOP value of the satellite's solar panel and the main body. The ranges of variation for the satellite's solar panel and the main body are 0–0.9 and 0–0.1, respectively.

4. When the incident sunlight angle is fixed, the aforementioned change in the incidence angle of sunlight is equivalent to a change in the attitude of the target. Based on the analysis results, we can analyze and determine the operating attitudes of the LEO space target by using the polarization characteristics.

IV. POLARIZATION CHARACTERISTICS OF THE LEO SPACE TARGETS WITH DIFFERENT MATERIAL PROPERTIES

Herein, we analyzed the scalar BRDF and DOP of different target materials, namely Al, Mg, and Ti. We consider a typical observation condition, as an example, where the sunlight's incident zenith angle θ_i is in the range $0^\circ - 85^\circ$, incident azimuth angle ϕ_i is 0° , and receiving direction angle (θ_r, ϕ_r) is $(45^\circ, 180^\circ)$. The analysis results are presented in Fig. 4. Because the scalar BRDF is proportional to the light intensity, its value can be used to directly reflect the light intensity characteristics.

The results in Fig. 4 were normalized to the results

obtained for Al to obtain the scalar BRDF and DOP contrasts, which are expressed, respectively, as

$$C_B = |B_{Al} - B_i|/B_i, \quad (7)$$

$$C_P = |P_{Al} - P_i|/P_i, \quad (8)$$

where B denotes the BRDF value, P denotes the DOP value, and i denotes the Mg and the Ti materials. The change in contrast between DOP and BRDF is given as follows

$$\Delta = (C_P - C_B) \times 100\%. \quad (9)$$

The calculated results are presented in Fig. 5. Figures 5(a) and 5(b) show that the DOP comparison results among different materials are significantly different than those of BRDF. Figure 5(c) shows that the contrast enhancement of DOP against BRDF was nearly 25%; therefore, in some cases, polarization was more effective than intensity for identifying the target materials. When different space target components exhibit an approximate reflectivity value owing to the properties of the surface materials and surface shape, intensity detection will not be able to distinguish between these components effectively. Polarization detection enhances the image contrast by measuring polarization information.

V. SIMULATION OF THE POLARIZATION IMAGING CHARACTERISTICS OF THE SPACE TARGETS

We developed visual simulation software for simulating the polarization imaging characteristics of space targets. First, we established a simulation model of the satellite target by using three-dimensional modeling software. The satellite model was provided as an input to the software and the geocentric coordinates (X_{MG} , Y_{MG} , Z_{MG}) of the satellite target were calculated according to the orbital elements of the target. Next, we determined the observatory center's coordinates (X_{MS} , Y_{MS} , Z_{MS}) of the satellite target as follows

$$\begin{bmatrix} X_{MS} \\ Y_{MS} \\ Z_{MS} \end{bmatrix} = R^{-1} \cdot \begin{bmatrix} X_{SG} - X_{MG} \\ Y_{SG} - Y_{MG} \\ Z_{SG} - Z_{MG} \end{bmatrix}, \quad (10)$$

where (X_{SG} , Y_{SG} , Z_{SG}) represents the geocentric coordinates of the observatory, which can be calculated from the geodetic coordinates (L_Z , B_Z , H_Z) of the observatory as follows

$$\begin{cases} X_{SG} = (N + H_Z) \cos B_Z \cos L_Z \\ Y_{SG} = (N + H_Z) \cos B_Z \sin L_Z \\ Z_{SG} = [N(1 - e^2) + H_Z] \sin B_Z \end{cases} \quad (11)$$

where N represents the radius of curvature of a unitary circle, e represents the first off-center rate, and R represents the coordinate transformation matrix illustrated

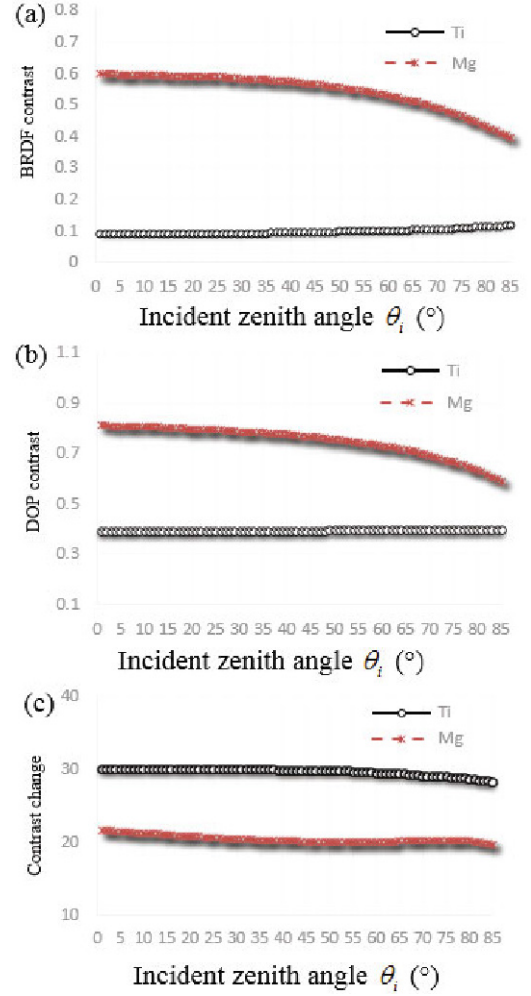


Fig. 5. (Color online) Analysis results for the (a) BRDF contrast, (b) DOP contrast, and (c) contrast change as functions of the incident zenith angle.

by the following expression:

$$R = \begin{bmatrix} \cos L_Z & -\sin L_Z & 0 \\ \sin L_Z & \cos L_Z & 0 \\ 0 & 0 & 1 \end{bmatrix} \times \begin{bmatrix} \cos(90 - B_Z) & 0 & \sin(90 - B_Z) \\ 0 & 1 & 0 \\ -\sin(90 - B_Z) & 0 & \cos(90 - B_Z) \end{bmatrix} \cdot \begin{bmatrix} 0 & -1 & 0 \\ 1 & 0 & 0 \\ 0 & 0 & 1 \end{bmatrix}. \quad (12)$$

Next, we considered the attitude, observation position, and light source position information of the space targets as inputs for constructing the observation environment. The polarization imaging characteristics of the target were calculated using the microfacet analysis model. Based on the visual simulation technology, which was combined with the optical observation parameters, such as the resolution of the detector $M \times N$, pixel size d , and focal length of the optical system f , we determined an observational view angle field of the imaging system

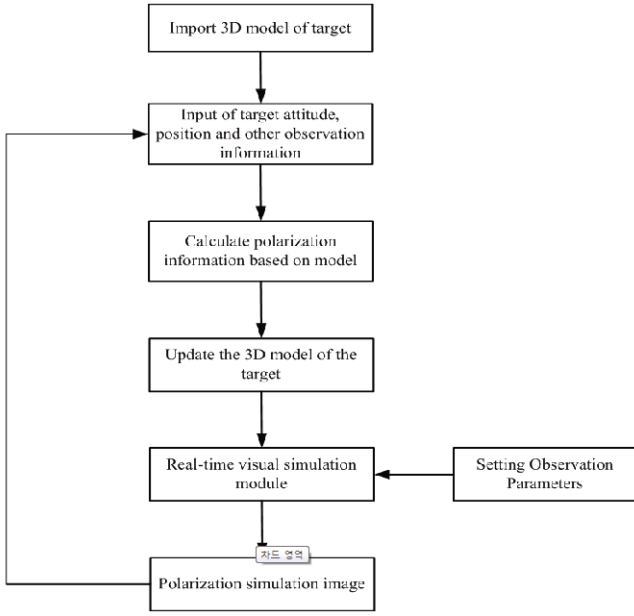


Fig. 6. Flow chart for the modeling and analysis of the space target polarization characteristics.

in both the horizontal and the vertical directions:

$$HFov = \arcsin\left(\frac{d}{f}\right) \times M, \quad (13)$$

$$VFov = \arcsin\left(\frac{d}{f}\right) \times N. \quad (14)$$

Finally, we simulated the polarization imaging effect of typical space targets based on the aforementioned parameters. The specific flow chart of the simulation is shown in Fig. 6 whereas the simulation images of typical space targets at different operating attitudes are shown in Fig. 7. In comparison with the light intensity images, the DOP images contribute to resolving the composition structure and improving the image resolution capacity of LEO space targets. The difference between the main body and the solar panel and that between different parts of the main body were more discernible in the polarization image.

VI. EXPERIMENT

Imaging the observation events of LEO space satellite targets on Earth is militarily sensitive, and satellite images are confidential. To avoid this problem, we conducted observational experiments of the satellite scale model laboratory and outfield aerial target.

The laboratory polarization detection system comprises a THOLARBS linear polarizer, imaging lens, and Hamamatsu SCMOS detector. THOLARBS polarizer was rotated at polarization angles of 0° , 45° , 90° , and

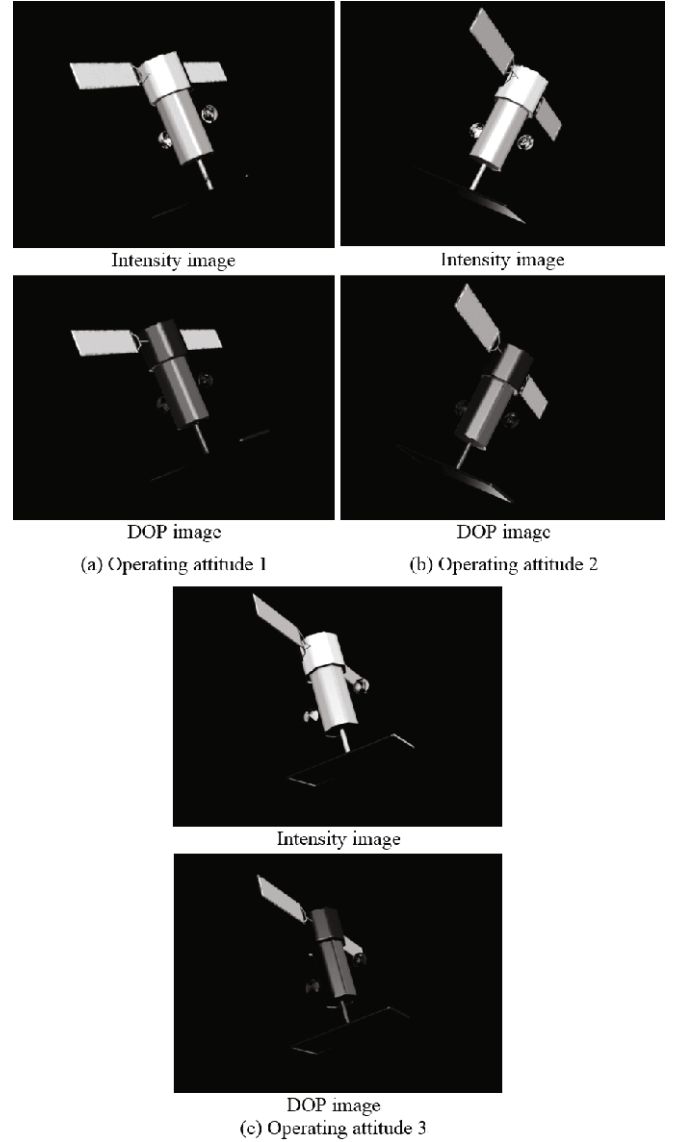


Fig. 7. Comparison of the simulation image effects under operating attitudes (a) 1, (b) 2, and (c) 3.

135° , the SCMOS detector correspondingly obtained images I_0 , I_{45} , I_{90} and I_{135} for each of the four paths. Based on polarization theory [27–29], we acquired the light intensity and the DOP images, as shown in Figs. 8(a) and 8(b), respectively.

The intensity values at different parts of the satellite exhibited obvious differences in the light intensity images therefore, when some pixels of the detector were close to saturation, and some parts of the target could not be identified. However, we could characterize the hidden area in the light intensity images by using the polarization method for target detection as a different characterization method. Therefore, the light intensity and the polarization images were combined, as shown in Fig. 8(c). As a result, the target's features could be completely expressed. Therefore, polarization can be an

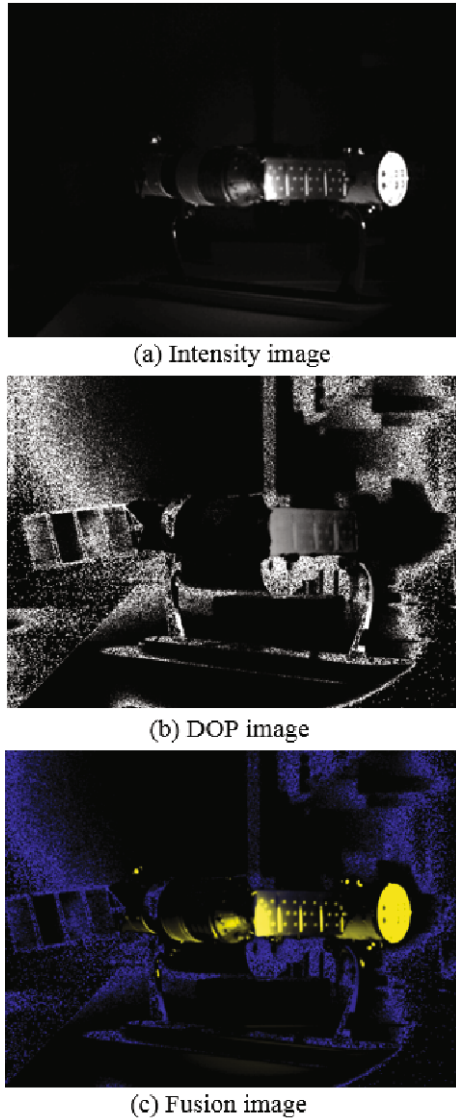


Fig. 8. (Color online) Results of the laboratory polarization imaging detection.

important complement to light intensity.

The outfield imaging detection system comprises an imaging lens, four-dimensional technology a polarization camera, and a two-dimensional tracking turntable, as shown in Fig. 9. An aircraft is the observation target of the outfield experiment, and the experimental results are shown in Fig. 10. While representing light information, a significant difference between the light intensity and the DOP images is shown in Fig. 10(a). If we assume the aircraft in Fig. 10(a) to be in a dark background of space, we may not be able to observe the wings in the light intensity image; however, we can observe them in the DOP images. The gray value of the wings is higher than that of the aircraft body, which is consistent with the laboratory experimental result. In addition, the profile of the polarization image was clearer than that of the



Fig. 9. (Color online) Outfield imaging detection system.

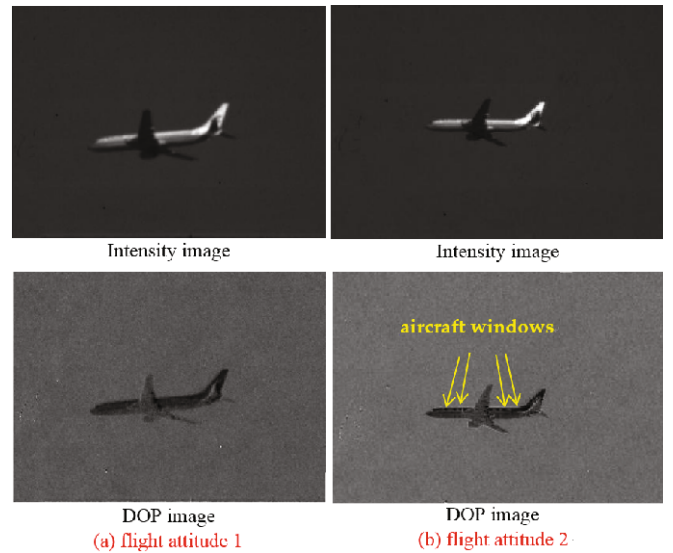


Fig. 10. (Color online) Comparison of the outfield image effects under flight attitudes (a) 1 and (b) 2.

light intensity image. From Fig. 10(b), we can observe that the light intensity image cannot distinguish between the aircraft's body and the windows, which is not the case in the DOP image. In particular, the DOP value of the aircraft's window was significantly lower than that of the main body, suggesting that, in some cases, the DOP image exhibited a better resolution corresponding to different constituent structures of the aircraft.

VII. CONCLUSION

Intensity, wavelength, coherence, and polarization are basic properties of an optical field. Herein, we focused on analyzing and investigating the polarization characteristics of space targets. In particular, we utilized a microfacet analysis model for analyzing the targets' polarization characteristics for different operating attitudes

and surface materials. The polarization image of a typical LEO space target was simulated for analyzing its effectiveness in resolving the compositional structure and improving the image resolution capacity. Furthermore, we established laboratory and outfield polarization detection experimental systems to observe the polarization images of different targets. The simulated and the experimental results demonstrated that (1) polarization is effective in analyzing and evaluating the operating attitudes of the LEO space targets; (2) polarization is effective in identifying the material properties of the LEO space targets; and (3) a polarization image is an effective tool for discriminating the constituent structure of LEO space targets. Based on these findings, we can state that polarization characteristics, as an important complement to the light intensity of LEO space targets, can be a sensible argument. Results provide basic data support for improving the effectiveness of LEO space target detection and recognition. Furthermore, they provide firsthand proof of the significance and advantages of LEO space target polarization imaging detection that may provide effective guidance for the demonstration and the design of a polarization image instrument for LEO space targets.

The conducted research exhibited the following limitations: (1) it is sensitive to study at the imaging characteristics of satellite targets, therefore, this research work can only analyze some of the existing public data, and (2) for outfield polarization experiments, only air targets can be used because of sensitivity problems. Although the imaging principle was consistent, the difference in optical information transmission paths between the space target and the air target will result in deviations in a real-time situation.

ACKNOWLEDGMENTS

The authors would like to thank Dr. Yao Kainan, Changchun Institute of Optics, Fine Mechanisms and Physics, for providing the satellite scale model and Dr. Wang Guocong and Dr. Li Tianci for their useful discussions and remarks. This research was supported by Fundamental Research Funds for the Central Universities (3132019141).

REFERENCES

- [1] N. Li, Y. Zhao, Q. Pan and S. G. Kong, *Opt. Express* **27**, 1376 (2019).
- [2] Z. Sun, D. Wu, Y. Lu and S. Lu, *IEEE T. Geosci. Remote* **57**, 4388 (2019).
- [3] L. Meng and J. P. Kerekes, *IEEE T. Geosci. Remote* **52**, 6615 (2014).
- [4] B. Kanseri and K. R. Sethuraj, *Opt. Lett.* **44**, 159 (2019).
- [5] T. Hu *et al.*, *Atmosphere* **10**, 342 (2019).
- [6] A-L. Sahlberg *et al.*, *Appl. Spectrosc.* **73**, 653 (2019).
- [7] M. Alizadeh, M. Ghotbi, P. Loza-Alvarez and D. Merino, *Methods Protoc.* **2**, 49 (2019).
- [8] B. Ben-Dor, U. P. Oppenheim and L. S. Balfour, in *Proceedings Volume 1971, 8th Meeting on Optical Engineering in Israel: Optical Engineering and Remote Sensing*; (1993), Event: 8th Meeting in Israel on Optical Engineering, 1992, Tel Aviv, Israel.
- [9] R. Nothdurft and G. Yao, *Opt. Express* **13**, 4185 (2005).
- [10] J. E. Solomon, *Appl. Optics* **20**, 1537 (1981).
- [11] W. Shen *et al.*, *Opt. Lett.* **43**, 1255 (2018).
- [12] X. Ju *et al.*, *Appl. Optics* **57**, 8600 (2018).
- [13] G. H. Sanders, *J. Astrophys. Astron.* **34**, 81 (2013).
- [14] S. Gunnels, “The Giant Magellan telescope (GMT): Gregorian instrument rotator bearing,” *Proc. SPIE* 91455E (2014).
- [15] Z. Huang, R. Huang and X. Xue, *Appl. Sci.* **8**, 2604 (2018).
- [16] X. Liang, J. Zhou and W. Ma, *Appl. Optics* **58**, 5136 (2019).
- [17] D. Zhang, Q. Y. Yang and T. Chen, *Appl. Optics* **58**, 4337 (2019).
- [18] R. Bourgois and R. Geyl, “Manufacturing ELT optics: Year 2 report,” 2019, Optical Fabrication and Testing, Paper# OM3A.3.
- [19] A. H. Bouchez *et al.*, in *Adaptive Optics Systems IV*, Vol. 9148, p. 91480W. International Society for Optics and Photonics, 2014, DOI: 10.1117/12.2057613.
- [20] X. Zhang *et al.*, *Opt. Express* **27**, 11651 (2019).
- [21] Y. Li, X. Xia and Y. M. Paulus, *Photonics* **5**, 9 (2018).
- [22] C. González-Gutiérrez *et al.*, *Sensors* **17**, 1263 (2017).
- [23] D. Li *et al.*, *Sensors* **17**, 785 (2017).
- [24] O. Korotkova, *Opt. Lett.* **40**, 3077 (2015).
- [25] G. Wang, J. Wang, Z. Zhang and W. Zeng, *Acta Photonica Sinica* **45**, 0410003-1 (2016).
- [26] R. G. Priest and S. R. Meier, *Opt. Eng.* **41**, 988 (2002).
- [27] X. Lu *et al.*, *Opt. Express* **26**, 2495 (2018).
- [28] A. M. Phenis, M. Virgen and E. E. de Leon, In *Novel Optical Systems Design and Optimization VIII* (Vol. 5875, p. 587502). International Society for Optics and Photonics.
- [29] J. Mudge, M. Virgen and P. Dean, In *Polarization Science and Remote Sensing IV* (Vol. 7461, p. 74610L). International Society for Optics and Photonics.